

EARLY STRUCTURE FORMATION FROM PRIMORDIAL DENSITY FLUCTUATIONS WITH A BLUE-TILTED POWER SPECTRUM

SHINGO HIRANO¹, NICK ZHU^{1,3}, NAOKI YOSHIDA^{1,2}, DAVID SPERGEL³, AND HAROLD W. YORKE⁴

Draft version December 20, 2021

ABSTRACT

While observations of large-scale structure and the cosmic microwave background (CMB) provide strong constraints on the amplitude of the primordial power spectrum (PPS) on scales larger than 10 Mpc, the amplitude of the power spectrum on sub-galactic length scales is much more poorly constrained. We study early structure formation in a cosmological model with a blue-tilted PPS. We assume that the standard scale-invariant PPS is modified at small length scales as $P(k) \sim k^{m_s}$ with $m_s > 1$. We run a series of cosmological hydrodynamic simulations to examine the dependence of the formation epoch and the characteristic mass of primordial stars on the tilt of the PPS. In models with $m_s > 1$, star-forming gas clouds are formed at $z > 100$, when formation of hydrogen molecules is inefficient because the intense CMB radiation destroys chemical intermediates. Without efficient coolant, the gas clouds gravitationally contract while keeping a high temperature. The protostars formed in such “hot” clouds grow very rapidly by accretion to become extremely massive stars that may leave massive black holes with a few hundred solar-masses at $z > 100$. The shape of the PPS critically affects the properties and the formation epoch of the first generation of stars. Future experiments of the CMB polarization and the spectrum distortion may provide important information on the nature of the first stars and their formation epoch, and hence on the shape of the small-scale power spectrum.

Subject headings: cosmology: theory – dark ages, reionization, primordial stars – stars: Population III – stars: formation – method: numerical

1. INTRODUCTION

The formation of the first stars marks the end of the cosmic Dark Ages, when their energetic photons initiates reionization of the inter-galactic medium. The exact epoch when cosmic reionization began is still uncertain, but evidence is mounting from an array of observations that the first luminous objects such as galaxies and quasars were formed very early on (Watson et al. 2015; Wu et al. 2015; Planck Collaboration XIII 2015). Wu et al. (2015) recently reported the discovery of a supermassive black hole in an extremely bright quasar. While their exact estimate of a black hole mass of twelve billion solar masses rests on the controversial use of broad emission lines (see e.g., Cackett et al. 2015), this ultra-luminous quasar must host a supermassive black hole. There are now over 40 quasars known with $z > 6$ including ULAS J1120+0641 with a $2 \times 10^9 M_\odot$ black hole at $z = 7.085$ (Mortlock et al. 2011; De Rosa et al. 2014) and a recently discovered $z = 6.889$ quasar with a black hole of $2.1 \times 10^9 M_\odot$ (De Rosa et al. 2014). Assembling these giant quasar hosts by this early epoch poses a serious challenge to the theory of structure formation and the growth of black holes.

There has been significant progress in the past decade in theoretical studies of the formation of the first generation of stars (see Bromm 2013; Glover 2013; Greif

2015, for recent reviews). Owing largely to the fact that the initial conditions are cosmologically well determined, one can perform *ab initio* simulations of early structure formation (e.g., Bromm et al. 2002; Abel et al. 2002; Yoshida et al. 2003). An important element of such simulations is the primordial power spectrum (PPS) from which a realistic initial density field can be generated in a fully cosmological context.

The PPS is observationally determined to have a power-law with a spectral index $n_s \simeq 0.96$ (Planck Collaboration XIII 2015). Unfortunately, such tight constraints are derived only at large length scales, up to the wavenumber of $k \simeq 0.2 \text{ Mpc}^{-1}$ (Hlozek et al. 2012). Most of theoretical studies thus assume a scale-invariant PPS and adopt significant extrapolation of the observationally determined large-scale power spectrum. The observational evidence on sub-galactic scales is confusing: milli-lensing measurements suggest substructure consistent with the extrapolation of the Λ -Cold Dark Matter (Λ -CDM) power spectrum to smaller scales (Hezaveh et al. 2013; Busmann et al. 2013; Xu et al. 2015) yet studies of local dwarf galaxies suggest significant problems with Λ -CDM on small scales (Strigari et al. 2007). It is not only interesting to explore how early structure formation is affected by enhanced density fluctuations at small scales, but also timely because the existence of supermassive black holes at very high redshifts suggests rapid growth of small scale structure in the early universe.

A variety of possibilities are proposed from the physics of the early universe that posit scale-dependent PPS. Popular single-field inflation models predict a nearly scale-free and slightly red power spectrum for adiabatic scalar perturbations. There are also variant models that predict scale-dependent power

¹ Department of Physics, University of Tokyo, Bunkyo, Tokyo 113-0033, Japan

² Kavli Institute for the Physics and Mathematics of the Universe (WPI), Institutes for Advanced Study, University of Tokyo, Kashiwa, Chiba 277-8583, Japan

³ Department of Astrophysical Sciences, Princeton University, Peyton Hall, Princeton, NJ 08544, USA

⁴ Jet Propulsion Laboratory, California Institute of Technology, Pasadena, CA 91109, USA

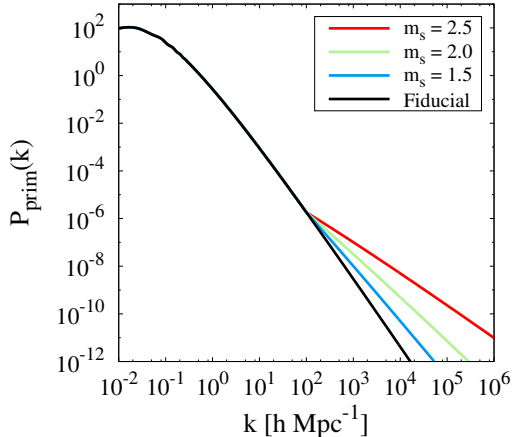


FIG. 1.— We plot the matter power spectra for the considered cases in the present paper with $k_p = 100 h \text{ Mpc}^{-1}$. The black line is for the scale-independent PPS (Eq. 1) whereas the other three lines show the scale-dependent models given by Eq. 2 with $m_s = 1.5$ (blue), 2.0 (green), and 2.5 (red), respectively.

spectrum with kinks, bumps, and other types of features (e.g., Starobinskij 1992; Adams et al. 1997; Kawaguchi et al. 2008; Biswas et al. 2010; Barnaby 2010). Of particular interest to us in the present paper are the models that generate density perturbations with a blue-tilted power spectrum or with enhancement at small length scales (Covi & Lyth 1999; Martin & Brandenberger 2001; Gong & Sasaki 2011).

It is naively expected that structure forms early in such models, yielding abundant small mass dark halos. Because primordial star formation involves a number of physical processes such as chemistry and radiative transfer as well as gravitational assembly of dark halos, the initial density perturbations or the PPS can affect the formation of primordial stars in a complicated manner. Clearly, it is important to study the properties of the first structure using cosmological simulations with the relevant physics included.

In the present paper, we perform a series of cosmological simulations for different PPS models to study early structure formation in detail. In particular, we examine how the slope of the PPS at the small length scales affects the formation epoch and the mass of the first generation of stars. We begin by describing the calculation methods in Section 2. Section 3 shows the simulation results of primordial star formation for different PPS models. We discuss the dependence of the primordial star formation on the PPS model in Section 4. Throughout this paper, we adopt the standard Λ -CDM cosmology with the total matter density $\Omega_m = 0.3086$, the baryon density $\Omega_b = 0.04825$, the dark energy density $\Omega_\Lambda = 0.6914$ in units of the critical density, the Hubble constant $h = 0.6777$, and the primordial index $n_s = 0.9611$ (Planck Collaboration XVI 2014).

2. NUMERICAL SIMULATIONS

We perform a series of cosmological simulations that start from the initial conditions generated for different PPS models $P_{\text{prim}}(k)$. In the next sections, we

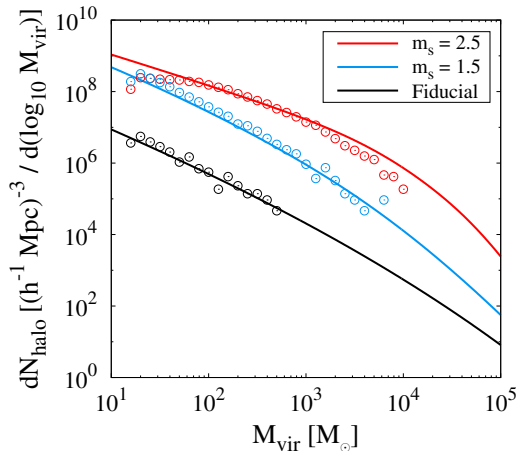


FIG. 2.— We compare the halo mass functions at $z = 100$ for three PPS models. We set the normalization parameter $\sigma_8 = 2.5$ here. The lines show the Press-Schechter mass functions, while the symbols show the results of our cosmological simulations with a volume of $60 h^{-1}$ comoving kilo-parsec on a side. We run the Friend-Of-Friend (FOF) halo finder with linking length $b = 0.2$ to obtain the halo mass functions.

describe the numerical methods with emphasis on the improvement over our earlier numerical simulations (Hirano et al. 2014, 2015).

2.1. Initial Conditions

The standard scale-invariant PPS is given by

$$P_{\text{prim}}(k) \propto k^{n_s}, \quad (1)$$

whereas the model power spectrum with enhancement at small scales is given by

$$P_{\text{prim}}(k) \propto k^{n_s} \quad (k < k_p), \\ \propto k_p^{n_s - m_s} \cdot k^{m_s} \quad (k > k_p). \quad (2)$$

We adopt two parameters that characterize the spectrum; k_p is the pivot wavenumber above which the spectral index is set to be m_s . We consider $k_p = 100, 300$, and $500 h \text{ Mpc}^{-1}$ and $m_s = 1.5, 2$, and 2.5 .

Figure 1 shows the matter power spectra for models with $k_p = 100 h \text{ Mpc}^{-1}$. The fiducial pure power-law PPS case is also shown there for comparison. We use the transfer function of Eisenstein & Hu (1999) for this plot and also for generating the initial conditions using the publicly available code MUSIC (Hahn & Abel 2011). The density fluctuation amplitude is normalized by σ_8 . Because our simulation volume is very small, we set σ_8 larger than the current standard value of about 0.8 (Planck Collaboration XIII 2015), so that we can simulate the formation of high- σ peak halos. In practice, we set $\sigma_8 = 1.5, 2$, and 2.5 . In total, we generate 18 cosmological initial conditions with the parameter sets given in Table 1.

The effect of the enhanced small-scale power is clearly seen in the mass function (Fig. 2). The halo mass functions differ by orders of magnitude at $z = 100$. Figure 2 also shows that the Press-Schechter mass function agrees fairly well with the simulation results (see also Reed et al. 2005).

TABLE 1
 PROPERTIES OF FIRST STAR FORMATION DEPENDING ON THE PPS MODELS

ID	σ_8	k_p ($h \text{ Mpc}^{-1}$)	m_s	z_{form}	M_{vir} ($10^5 M_\odot$)	M_{Jeans} (M_\odot)	\dot{M}_{Jeans} ($10^{-3} M_\odot \text{ yr}^{-1}$)	$M_{*,\text{cal}}$ (M_\odot)	$M_{*,\text{est}}$ (M_\odot)
100	1.5	–	–	24.0	2.17	45	0.63	45	88
111		100	1.5	27.1	1.82	162	2.97		261
112			2.0	36.1	0.88	162	1.16		135
113			2.5	87.9	0.31	69	0.77	96	101
131		300	1.5	24.0	2.11	23	0.24		45
132			2.0	25.2	2.19	124	0.74		98
133			2.5	33.9	1.97	171	3.31		281
151		500	1.5	23.5	2.10	33	0.35		58
152			2.0	24.0	2.19	61	1.02		123
153			2.5	27.1	2.83	90	1.61		170
200	2.0	–	–	34.9	1.30	401	1.54	114	165
211		100	1.5	40.1	0.83	167	1.29		145
212			2.0	53.2	0.22	57	0.25		46
213			2.5	138.2	0.24	142	1.71	145	177
300	2.5	–	–	46.2	0.83	243	2.34	118	220
311		100	1.5	52.6	0.65	164	1.39		153
312			2.0	72.1	0.22	60	0.43		67
313			2.5	186.3	0.37	411	2.72	362	245

NOTE. — Column 1: Cloud index, Column 2 – 4: PPS model parameters, Column 5 – 8: Properties of star-forming clouds, Column 9: Stellar mass calculated by RHD simulations, and Column 10: Stellar mass estimated by a fitting formula (9). The cloud ID indicates the combination of the three parameters $\{\sigma_8, k_p, m_s\}$.

2.2. Cosmological Simulations

We perform the cosmological simulations using the parallel N-body / Smoothed Particle Hydrodynamics (SPH) code Gadget-2 (Springel 2005) suitably modified for the primordial star formation simulations (Yoshida et al. 2006, 2007; Hirano et al. 2014, 2015). In order to achieve sufficient numerical resolution, we use hierarchical zoom initial conditions. The parent simulation volume is $L_{\text{box}} = 100 h^{-1} \text{ kpc}$ on a side. The mass of the refined dark matter particles in the zoomed region is $0.80 M_\odot$, and that of the baryonic component is $0.15 M_\odot$. We follow structure formation from $z_{\text{ini}} = 499$ until the central hydrogen number density reaches $n_{\text{H, cen}} \simeq 10^7 \text{ cm}^{-3}$ or 10^{13} cm^{-3} in a gas cloud that first collapses (see Section 2.3). The initial ionization fraction is computed by using RECFAST (Seager et al. 1999, 2000; Wong et al. 2008) as $x_e = 6.88 \times 10^{-4}$ at the initial redshift. During the cloud collapse, we keep the refinement criterion that the local Jeans length is always resolved by 15 times the local smoothing length by progressively increasing the spatial resolution by the particle-splitting technique (Kitsionas & Whitworth 2002).

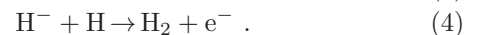
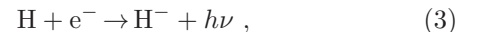
Let us briefly describe the overall trend found from the simulation result. In the standard model, the first stars are formed at $z \sim 20 - 50$ (e.g., Tegmark et al. 1997; Reed et al. 2005; Yoshida et al. 2003). In one of our simulations with $\sigma_8 = 1.5$, the first star is formed at $z_{\text{form}} = 24$ within the simulation volume of $100 h^{-1} \text{ kpc}$ on a side. We label this sample as ID 100. Here, the first digit “1” indicates the value of σ_8 (see Table 1). We also find that, by changing σ_8 to 2.0 and 2.5 (ID = 200 and 300), the first star in the simulation volume is formed earlier at $z_{\text{form}} = 35$ and 46, respectively.

2.2.1. H_2 Formation in the Early Universe

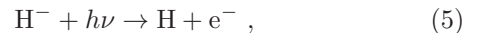
We are interested in the thermal evolution of a primordial gas cloud formed at $z > 100$. Because CMB

photons at such high redshifts are capable of dissociating molecules and ions, several chemical reactions need to be included in order to follow the thermal and chemical evolution accurately.

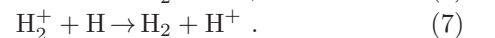
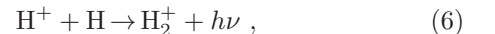
At $z < 100$, the main H_2 formation path is the so-called H^- channel;



Because H^- ions are destroyed by CMB photons at $z > 100$ via the photo-detachment reaction



the H^- channel is not effective at such early epochs. An alternative path is the H_2^+ channel:



An opposing dissociative process by energetic photons operates as



At $z > 120$, most of the hydrogen molecules are formed by the H_2^+ channel. The mean H_2 fraction in the Universe reaches $\sim 10^{-6}$ at $z \sim 60$. We update the chemical network by introducing the above reactions (see a review by Galli & Palla 2013). The reaction rates are based on Coppola et al. (2013). We describe more details of the chemistry implementation in Appendix A.

2.3. Final Stellar Masses

It is important to study the characteristic mass of the first stars in our variant cosmological models with blue-tilted PPS. We calculate the mass of a primordial star by using two different methods. One is direct calculation of gas accretion onto the central protostar us-

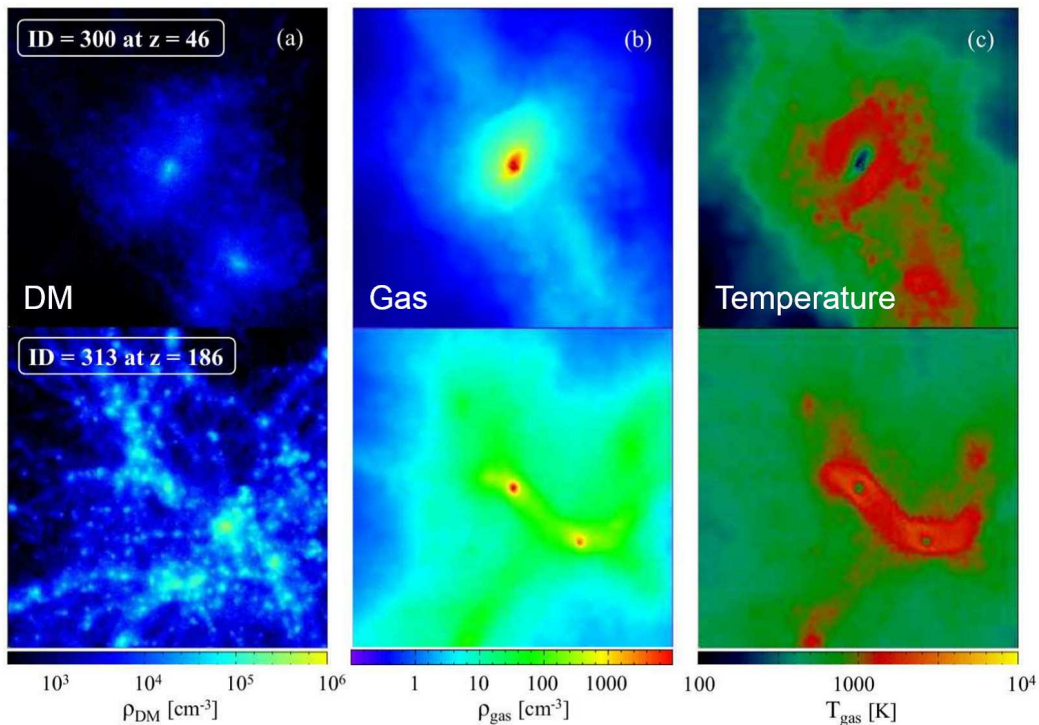


FIG. 3.— Projected densities for dark matter (Panel a) and baryonic components (b). We also plot the projected gas temperature (c) at the formation sites of the primordial stars ID 300 (top; $z_{\text{form}} = 46$) and ID 313 (bottom; $z_{\text{form}} = 186$). The plotted region has a proper 100 pc on a side. We scale the density in units of particle number density per cubic-centimeter.

ing the two-dimensional axisymmetric radiation hydrodynamic (RHD) simulation coupled with the stellar evolution (Hosokawa et al. 2011, 2012; Hirano et al. 2014, 2015). We perform the calculations for 6 cases. We label them as ID = 100, 113, 200, 213, 300, and 313. Here, the second digit of the object ID indicates the pivot wavenumber, and the last digit indicates the value of m_s (see Table 1). For each gas cloud, we generate the initial conditions for the RHD simulation by suitably mapping the final snapshot of our cosmological simulation at the time when the density of the collapsing cloud core reaches $n_{\text{H, cen}} = 10^{13} \text{ cm}^{-3}$. The RHD simulations are run until the mass accretion rate onto the central star falls below $10^{-4} M_{\odot} \text{ yr}^{-1}$. At this point the stellar growth is almost completely halted and the resultant mass can be regarded as the final stellar mass. We denote the stellar masses calculated directly by the RHD simulation as $M_{*, \text{cal}}$.

We also estimate the final stellar masses by using a fitting function that is derived from a number of RHD simulations of accreting protostars in our earlier studies. The fitting function essentially correlates the stellar mass $M_{*, \text{est}}$ to the gas infall rate \dot{M}_{Jeans} evaluated for a gravitationally Jeans unstable gas cloud. It is given by Hirano et al. (2015) as

$$M_{*, \text{est}} = 250 \left(\frac{\dot{M}_{\text{Jeans}}}{2.8 \times 10^{-3} M_{\odot} \text{ yr}^{-1}} \right)^{0.7} M_{\odot}. \quad (9)$$

By adopting this formula, we can skip the numerically costly RHD simulation in the accretion phase. Note that the difference between the calculated and estimated values is about fifty percent, and mostly within a factor of

two (see fig. 14b in Hirano et al. 2014). Although this might still appear insufficient to determine the stellar mass for all the cases in Table 1, the mass variations caused by model parameters (k_p , m_s , etc) are typically larger than the uncertainty in the estimated mass (see Table 1). Because we aim at investigating how cosmological parameters such as the slope of the power spectrum affect the formation of early halos and gas clouds, it would be clearer to interpret the resulting stellar masses in terms of gas clouds' properties such as the Jeans mass and accretion rate. Therefore, we use the estimated stellar masses (Eq. [9]) for all the 18 cases to discuss the qualitative dependence on the adopted PPS models.

Our stellar mass estimates are based on the results of radiation-hydrodynamics simulations which follow only the evolution of the central star. Recent three-dimensional simulations show that the circumstellar disk can gravitationally fragment to produce multiple clumps (sink particles; e.g., Clark et al. 2011; Greif et al. 2011, 2012; Stacy & Bromm 2013). Such fragments, if some of them survive over a long period of disk accretion, would form multiple stars with correspondingly small masses. High-resolution simulations show also that fragments efficiently merge onto the central star in roughly an orbital timescale (e.g., Greif et al. 2012; Vorobyov et al. 2013). In the latter case, the final stellar mass would be similar with the calculated value by our radiation-hydrodynamics simulation. Conservatively, we interpret the derived M_* as the total mass of stars formed, rather than the mass of a single star.

3. RESULTS

3.1. Major Effects

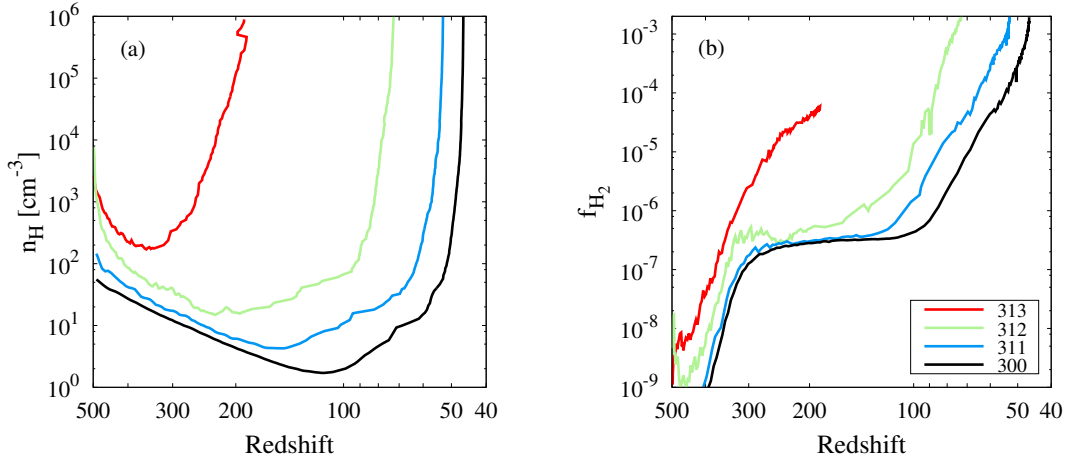


FIG. 4.— Time evolution of gas density (Panel a) and H_2 molecule fraction (Panel b) of the densest gas elements for cases with $\sigma_8 = 2.5$ until $n_{\text{H, cen}} = 10^6 \text{ cm}^{-3}$. The lines with different colors represent the four PPS models in Table 1.

We find major effects of the small-scale power spectrum on the properties of host halos and on the star formation within them. Figure 3 shows the local conditions around the formation site of the primordial star. The top panels are for the case with normal scale-invariant PPS (ID 300). The primordial star-forming cloud is formed at $z_{\text{form}} = 46$ inside a dark matter mini-halo that has a virial radius of $R_{\text{vir}} \simeq 19 \text{ pc}$. The bottom panels are for the case with an extremely enhanced PPS (ID 313). The gas cloud is formed earlier at $z_{\text{form}} = 186$ inside a more compact mini-halo with $R_{\text{vir}} \simeq 3.6 \text{ pc}$. Figure 3(a) shows the density distribution of dark matter component within a proper 100 pc on a side. Note that the mean density is higher in the bottom case than in the top because of the cosmic expansion, as $\rho \propto (1+z)^3$. The number of small mass dark matter clumps is significantly larger in the bottom panel, reflecting the enhanced initial density perturbations at the corresponding length scales (e.g., Figs. 1 and 2). Interestingly, we find a secondary star-forming cloud formed in the vicinity of the first one within several 10 pc (Fig. 3b). Such a close pair of primordial stars likely affect each other through radiative, dynamical, and chemical feedback effects. In the top panels, we also find a neighboring mini-halo but it has not grown sufficiently to host a dense star-forming cloud (see also the temperature distribution in Panel c).

The host mini-halos forming at very high redshifts are generally more compact and have larger dark matter densities, whereas the characteristic density of the gas cloud is determined largely by molecular hydrogen cooling. Consequently, the baryonic component becomes dynamically dominant only after the gas density exceeds $\simeq 10^5 \text{ cm}^{-3}$ in very early halos.

3.2. Formation Epoch and H_2 Formation

Figure 4(a) shows the density evolution of the gas cloud’s core as a function of redshift for the cases with $\sigma_8 = 2.5$. With more enhanced power (larger m_s), the clouds collapse earlier. In the extreme case with $m_s = 2.5$ (red line), the cloud collapses at $z \sim 186$. Then H_2 formation mainly proceeds via the H_2^+ channel, but

the photo-dissociation by CMB prevents H_2 formation. Hence the molecular fraction remains low for ID 313 until three-body H_2 formation operates at very high densities (Fig. 4b). The formation of H_2 molecules critically affects the thermal evolution, prestellar collapse, and the subsequent accretion process onto the central protostar.

3.3. Thermal and Dynamical Properties of Clouds

Figure 5 shows the evolution and the properties of collapsing clouds for the six cases for which direct RHD simulations are performed. We use black lines for models with the standard power-law spectrum ($m_s = n_s$) and we use red lines for models with enhanced small scale power ($m_s > 1$). The thermal evolution in the standard model is well understood and can be described as follows (see Panel a). The temperature first increases due to gravitational contraction but then decreases owing to H_2 cooling, when the molecular fraction reaches the critical value that is needed to cool the gas within a Hubble time $f_{\text{H}_2} \simeq 5 \times 10^{-4}$ (see Fig. 5b, e.g., Tegmark et al. 1997). Note that the minimum temperature is floored by T_{CMB} at high redshifts. The gas temperature starts increasing again when the compressional heating overcomes the radiative cooling, leading to the formation of a protostar.

In our models with enhanced small scale power (red lines), the cloud evolves on a higher temperature track because of the lower H_2 fraction (Panel b). With larger m_s , the density at which the H_2 fraction reaches the critical value for cooling is larger. Interestingly, for ID 313 (red solid line), the H_2 fraction does not reach the critical value until three-body H_2 formation occurs at $n_{\text{H, cen}} > 10^8 \text{ cm}^{-3}$. In this case, the temperature at the onset of run-away collapse is 700 K, much higher than that found in the usual primordial star formation. One can naively expect that protostars formed in such a ‘hot’ cloud will grow very rapidly.

The stellar mass can be estimated from Eq. (9). Effectively, the mass accretion history determines the protostellar evolution and the strength of radiative feedback that halts the accretion of surrounding medium. Figure 5(c) shows the gas infall rate as a function of the

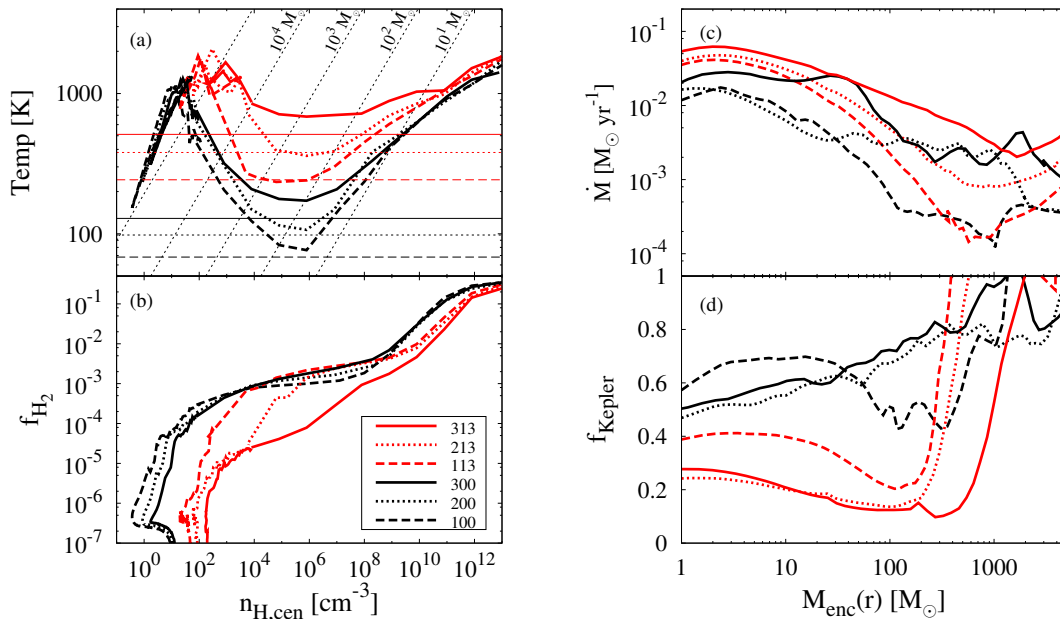


FIG. 5.— The evolution of temperature (Panel a) and H_2 fraction (Panel b) at the center of the cloud. The horizontal lines in Panel (a) indicate the CMB temperature, $T_{\text{CMB}}(z) = 2.73(1+z)$, at the respective formation epoch z_{form} listed in Table 1. The dotted lines show the Jeans mass for $10 - 10^5 M_{\odot}$ in the density-temperature plane. Panels (c) and (d) display the profiles of the instantaneous gas infall rate and the degree of rotational support ($f_{\text{Kepler}} = v_{\text{rot}}/v_{\text{Kepler}}$) as a function of the enclosed mass. The profiles are calculated when the cloud core density reaches $n_{\text{H, cen}} = 10^{13} \text{ cm}^{-3}$.

enclosed gas mass. On average, the gas infall rate systematically increases at higher redshift (see the difference from long-dashed to solid lines). However, the gas infall rate does not monotonically increase with m_s . This is because the host mini-halos of the gas clouds are formed at earlier epochs but contain less amount of gas.

Figure 5(d) shows the ratio of rotational speed to the Keplerian speed. Interestingly the gas clouds formed at earlier epochs spin significantly more slowly in the models with enhanced power. This may reflect the effective redistribution of the (orbital) angular momenta brought in by numerous minor mergers. Stars formed in a gas cloud with less spin tend to be more massive because of relatively rapid spherical accretion onto the protostar (Hirano et al. 2014).

3.4. Dependence on Model Parameters

It is important to study the effect of the pivot scale k_p of the PPS on gas cloud formation. There is an important physical scale that characterizes primordial star formation. Let us denote the characteristic wavenumber k_{halo} for a mini-halo that has a physical size R_{halo} so that $k_{\text{halo}} \sim 2\pi/R_{\text{halo}}$. When k_p is smaller than k_{halo} , the enhanced power generates more structure of mini-halo sizes.

In the fiducial case of ID = 100, the host halo has a virial mass of $\sim 2 \times 10^5 M_{\odot}$. The corresponding wavenumber is $k_{\text{halo}} = 2\pi/R_{\text{halo}} \sim 500 h \text{ Mpc}^{-1}$. When k_p is comparable to k_{halo} , as in the cases with $k_p = 300$ and $500 h \text{ Mpc}^{-1}$, increasing m_s does not significantly affect z_{form} and M_{vir} (see Table 1). This is in direct contrast to the trend found when $k_p < k_{\text{halo}}$; increasing m_s

actually resulted in *larger* z_{form} and *smaller* M_{vir} . This can be understood as follows. The formation epoch is largely determined by the amplitude of large-scale density perturbations whereas the enhanced power promotes formation of small mass halos. Therefore, when k_p is small, density perturbations at all the relevant length scales are enhanced. The mini-halos are then formed early, and are physically compact.

It is worth considering possible halo-to-halo variation. Our understanding so far is based on a limited number of samples. Hirano et al. (2014, 2015) show substantial differences in the properties of star-forming clouds even with similar masses and similar formation epochs that are in turn determined largely by the cosmological parameters. In principle, using a much large number of halos could show the general trend and variations more clearly, but we have focused on qualitative differences caused by the shape of PPS.

4. DISCUSSION

We have studied how the shape of the primordial power spectrum at small scales affects early structure formation. For a significantly enhanced PPS, star-forming gas clouds are formed at extremely early epochs of $z > 100$ (ID 213 and 313), when the usual gas-phase reaction of molecular hydrogen formation does not operate. At $100 < z < 300$, hydrogen molecules are formed via the H_2^+ channel and thus the gas can still cool and condense to form primordial stars. The formed stars have masses as large as $\sim 300 M_{\odot}$.

At even earlier epochs of $z > 300$, there is no efficient formation channel of H_2 and the possible path to

star formation is through cooling by atomic hydrogen. If the highly enhanced density perturbations, as explored in the present paper, grow quickly to form primordial gas clouds in the very early universe, an extremely massive star might be formed in a similar manner to the so-called direct collapse black hole formation model (e.g., Inayoshi et al. 2014). Such very massive stars gravitationally collapse to form remnant massive black hole at the end of their lives, leaving promising “seeds” for the formation of the recently discovered supermassive black hole (SMBH; Wu et al. 2015).

There is an additional generic physical process that can significantly affect the structure formation in the early universe; the relative motions between dark matter and baryons caused by acoustic oscillations at the cosmic recombination era (Tseliakhovich & Hirata 2010). The relative streaming motions prevent the gas contraction into dark matter mini-halo and delay the star formation, and thus possibly change the physical condition of the first star formation (see Fialkov 2014, for recent review). The effect is important at the very high redshifts considered in this paper, since the root-mean-square streaming velocity scales with redshift as $\propto (1+z)$. We have run several additional simulations and confirmed that, under significant streaming motions, primordial gas clouds are formed later in large host halos than presented in the present paper. There is an interesting possibility that streaming motions delay the first star formation to the extent that gas collapse is suppressed in mini-halos and more massive halos eventually host very massive stars, which can become the seed of SMBH (Tanaka & Li 2014). The blue-tilted primordial power-spectral can effectively increase the number of massive halos in the early universe. Further results from simulations with the streaming motions will be presented elsewhere (Hirano et al., in preparation).

Observationally, an independent probe of the PPS at small length scales might be provided by the existence of small mass dark halos in and around galaxies. Following the analytical model of Zhao et al. (2005), we estimate that an extremely large number of halos with masses of $\sim 1 M_{\odot}$ are formed for $m_s = 1.5$ and $k_p = 100 \text{ Mpc}^{-1}$. The typical formation epoch of such solar-mass halos is $z \sim 300$, and thus the halos may remain as very compact objects. However, even the dense and compact clumps can be destroyed by tidal stripping/disruption and en-

counter with stars in the Galaxy. It is thus difficult to estimate the abundance of the mini- and micro-halos surviving until today, either by large scale simulation (e.g., Diemand et al. 2005; Green & Goodwin 2007) or by analytical calculation (Zhao et al. 2005). Nevertheless, if signatures of small mass dark halos are detected through, for instance, dark matter annihilation or direct detection experiments, one can obtain invaluable information on their origin, i.e., the small-scale power spectrum.

Currently, there are little direct probes of the small-scale primordial density fluctuations, and only model dependent constraints are available (Chluba et al. 2012; Berezhinsky et al. 2014; Natarajan et al. 2015). We look forward to future CMB experiments such as PRISM⁵ and PIXIE (Kogut et al. 2011) that can infer the formation epoch and the spectral energy distribution (hence roughly the typical mass) of the first stars through measurement of CMB spectral distortions and the detection of low level of early reionization at $l > 10$ (e.g., Ricotti et al. 2005). Finally, James Webb Space Telescope (Windhorst et al. 2009) and WFIRST observations (Spergel et al. 2015) will probe the existence of quasars at even higher redshifts. Understanding the nature of the first stars may thus provide a route to probe observationally the small-scale primordial power spectrum.

We thank Jens Chluba and Carla Maria Coppola for helpful advices about chemistry implementations. We also thank Takashi Hosokawa, Kazuyuki Omukai and Teruaki Suyama for discussions and comments on the earliest star formation. NZ is grateful for the hospitality of Department of Astrophysical Sciences at Princeton University. NZ’s visit was supported by the University of Tokyo-Princeton strategic partnership grant. The numerical calculations were carried out on Cray XC30 and the general-purpose PC farm at Center for Computational Astrophysics, CfCA, of National Astronomical Observatory of Japan. This work was supported by Grant-in-Aid for JSPS Fellows (SH). and by the JSPS Grant-in-Aid for Scientific Research 25287050 (NY). Portions of this research were conducted at the Jet Propulsion Laboratory, California Institute of Technology, operating under a contract with the National Aeronautics and Space Administration (NASA).

REFERENCES

- Abel, T., Bryan, G. L., & Norman, M. L. 2002, *Science*, 295, 93
 Adams, J. A., Ross, G. G., & Sarkar, S. 1997, *Nuclear Physics B*, 503, 405
 Barnaby, N. 2010, *Phys. Rev. D*, 82, 106009
 Berezhinsky, V. S., Dokuchaev, V. I., & Eroshenko, Y. N. 2014, *Physics Uspekhi*, 57, 1
 Biswas, T., Mazumdar, A., & Shafieloo, A. 2010, *Phys. Rev. D*, 82, 123517
 Bromm, V. 2013, *Reports on Progress in Physics*, 76, 112901
 Bromm, V., Coppi, P. S., & Larson, R. B. 2002, *ApJ*, 564, 23
 Bussmann, R. S., Pérez-Fournon, I., Amber, S., et al. 2013, *ApJ*, 779, 25
 Cackett, E. M., Gültekin, K., Bentz, M. C., et al. 2015, *ApJ*, 810, 86
 Chluba, J., Erickcek, A. L., & Ben-Dayan, I. 2012, *ApJ*, 758, 76
 Clark, P. C., Glover, S. C. O., Smith, R. J., et al. 2011, *Science*, 331, 1040
 Coppola, C. M., Galli, D., Palla, F., Longo, S., & Chluba, J. 2013, *MNRAS*, 434, 114
 Coppola, C. M., Longo, S., Capitelli, M., Palla, F., & Galli, D. 2011, *ApJS*, 193, 7
 Covi, L., & Lyth, D. H. 1999, *Phys. Rev. D*, 59, 063515
 De Rosa, G., Venemans, B. P., Decarli, R., et al. 2014, *ApJ*, 790, 145
 Diemand, J., Moore, B., & Stadel, J. 2005, *Nature*, 433, 389
 Eisenstein, D. J., & Hu, W. 1999, *ApJ*, 511, 5
 Fialkov, A. 2014, *International Journal of Modern Physics D*, 23, 30017
 Galli, D., & Palla, F. 1998, *A&A*, 335, 403
 —. 2013, *ARA&A*, 51, 163
 Glover, S. 2013, in *Astrophysics and Space Science Library*, Vol. 396, *Astrophysics and Space Science Library*, ed. T. Wiklund, B. Mobasher, & V. Bromm, 103
 Gong, J.-O., & Sasaki, M. 2011, *JCAP*, 3, 28
 Green, A. M., & Goodwin, S. P. 2007, *MNRAS*, 375, 1111
 Greif, T. H. 2015, *Computational Astrophysics and Cosmology*, 2, 3
 Greif, T. H., Bromm, V., Clark, P. C., et al. 2012, *MNRAS*, 424, 399

⁵ <http://www.prism-mission.org/>

- Greif, T. H., Springel, V., White, S. D. M., et al. 2011, *ApJ*, 737, 75
- Hahn, O., & Abel, T. 2011, *MNRAS*, 415, 2101
- Hezaveh, Y., Dalal, N., Holder, G., et al. 2013, *ApJ*, 767, 9
- Hirano, S., Hosokawa, T., Yoshida, N., Omukai, K., & Yorke, H. W. 2015, *MNRAS*, 448, 568
- Hirano, S., Hosokawa, T., Yoshida, N., et al. 2014, *ApJ*, 781, 60
- Hirata, C. M., & Padmanabhan, N. 2006, *MNRAS*, 372, 1175
- Hlozek, R., Dunkley, J., Addison, G., et al. 2012, *ApJ*, 749, 90
- Hosokawa, T., Omukai, K., Yoshida, N., & Yorke, H. W. 2011, *Science*, 334, 1250
- Hosokawa, T., Yoshida, N., Omukai, K., & Yorke, H. W. 2012, *ApJ*, 760, L37
- Inayoshi, K., Omukai, K., & Tasker, E. 2014, *MNRAS*, 445, L109
- Kawaguchi, T., Kawasaki, M., Takayama, T., Yamaguchi, M., & Yokoyama, J. 2008, *MNRAS*, 388, 1426
- Kitsionas, S., & Whitworth, A. P. 2002, *MNRAS*, 330, 129
- Kogut, A., Fixsen, D. J., Chuss, D. T., et al. 2011, *JCAP*, 7, 25
- Martin, J., & Brandenberger, R. H. 2001, *Phys. Rev. D*, 63, 123501
- Mortlock, D. J., Warren, S. J., Venemans, B. P., et al. 2011, *Nature*, 474, 616
- Natarajan, A., Zhu, N., & Yoshida, N. 2015, *ArXiv e-prints*, arXiv:1503.03480
- Planck Collaboration XIII. 2015, *ArXiv e-prints*, arXiv:1502.01589
- Planck Collaboration XVI. 2014, *A&A*, 571, A16
- Reed, D. S., Bower, R., Frenk, C. S., et al. 2005, *MNRAS*, 363, 393
- Ricotti, M., Ostriker, J. P., & Gnedin, N. Y. 2005, *MNRAS*, 357, 207
- Seager, S., Sasselov, D. D., & Scott, D. 1999, *ApJ*, 523, L1
- . 2000, *ApJS*, 128, 407
- Spergel, D., Gehrels, N., Baltay, C., et al. 2015, *ArXiv e-prints*, arXiv:1503.03757
- Springel, V. 2005, *MNRAS*, 364, 1105
- Stacy, A., & Bromm, V. 2013, *MNRAS*, 433, 1094
- Starobinskij, A. A. 1992, *Soviet Journal of Experimental and Theoretical Physics Letters*, 55, 489
- Strigari, L. E., Bullock, J. S., Kaplinghat, M., et al. 2007, *ApJ*, 669, 676
- Tanaka, T. L., & Li, M. 2014, *MNRAS*, 439, 1092
- Tegmark, M., Silk, J., Rees, M. J., et al. 1997, *ApJ*, 474, 1
- Tselikhovich, D., & Hirata, C. 2010, *Phys. Rev. D*, 82, 083520
- Vorobyov, E. I., DeSouza, A. L., & Basu, S. 2013, *ApJ*, 768, 131
- Watson, D., Christensen, L., Knudsen, K. K., et al. 2015, *Nature*, 519, 327
- Windhorst, R. A., Mather, J., Clampin, M., et al. 2009, in *Astronomy*, Vol. 2010, astro2010: The Astronomy and Astrophysics Decadal Survey, 317
- Wong, W. Y., Moss, A., & Scott, D. 2008, *MNRAS*, 386, 1023
- Wu, X.-B., Wang, F., Fan, X., et al. 2015, *Nature*, 518, 512
- Xu, D., Sluse, D., Gao, L., et al. 2015, *MNRAS*, 447, 3189
- Yoshida, N., Abel, T., Hernquist, L., & Sugiyama, N. 2003, *ApJ*, 592, 645
- Yoshida, N., Oh, S. P., Kitayama, T., & Hernquist, L. 2007, *ApJ*, 663, 687
- Yoshida, N., Omukai, K., Hernquist, L., & Abel, T. 2006, *ApJ*, 652, 6
- Zhao, H., Taylor, J. E., Silk, J., & Hooper, D. 2005, *ArXiv e-prints*, arXiv:astro-ph/0502049

APPENDIX

A. REACTION RATE CALCULATION OF H_2^+ PHOTO-DISSOCIATION

The reaction rate calculation of H_2^+ photo-dissociation is highly uncertain. In our previous calculations (Hirano et al. 2014, 2015), we adopt the fitting function of Galli & Palla (1998) assuming the LTE-level population. The accurate reaction rate can be calculated by considering the H_2^+ -level population (Hirata & Padmanabhan 2006; Coppola et al. 2011). The time evolution of H_2 abundance at $z > 60$, which is the relevant epoch in our study, differs significantly depending on the adopted reaction rate (see fig. 3a in Galli & Palla 2013). We take a straightforward approach by comparing simulations with different reaction rates. Fortunately, we find that the uncertainty in the reaction rate gives essentially no influence on the primordial star formation. Stars are formed in dense gas clouds in which a critical amount of hydrogen molecules are formed to overcome the compressional heating by their radiative cooling. When a gas cloud becomes gravitationally unstable after the so-called loitering phase, the H_2 fraction within the cloud reaches a threshold value that is independent on the treatment of H_2^+ photo-dissociation. We thus adopt the LTE rate to produce the main results in the present paper. In most cases, we find a constant “floor” of the H_2 fraction at 2×10^{-7} owing to the H_2 formation via the H_2^+ channel (Fig. 4b).